Supplemental Material

Synthesis, structures, magnetic, and theoretical investigations of layered Co and Ni thiocyanate coordination polymers

Stefan Suckert, Michał Rams, Michael Böhme, Luzia S. Germann, Robert E. Dinnebier, Winfried Plass, Julia Werner and Christian Näther

Content

Table S1. Selected crystal data for compounds **1-Ni** and **2-Ni** obtained by single crystal X-ray analysis.

Compound	**1-Ni**	**2-Ni**
Formula	$C_{34}H_{36}N_6NiO_8S_2$	$C_{18}H_{18}N_4NiO_4S_2$
MW / g mol^{-1}	779.52	477.19
Crystal system	Monoclinic	Monoclinic
Space group	$P2_1$	$P2_1/c$
a / Å	11.0327(3)	14.8063(9)
b / Å	14.2185(3)	9.5965(3)
c / Å	11.9259(4)	15.7820(8)
α / °	90	90
β / °	95.618(2)	113.010(4)
γ / °	90	90
V / Å^3	1861.81(9)	2064.03(18)
T / K	170	200
Z	2	4
D_{calc} / g cm^{-3}	1.390	1.536
μ / mm^{-1}	0.690	1.175
θ_{max} / deg	27.350	27.242
Measured refl.	27836	29475
Unique refl.	8365	4603
Refl. [$F_0>4\sigma(F_0)$]	7689	3878
Parameter	502	353
R_{int}	0.0528	0.0741
R_1 [$F_0 > 4\sigma F_0$)]	0.0305	0.0497
wR_2 [all data]	0.0767	0.1162
GOF	1.064	1.084
$\Delta\rho_{max}$, $\Delta\rho_{min}$ / e Å^{-3}	0.269/ −0.320	0.391/ −0.464

Table S2. Selected crystal data and details of the Rietveld refinements for compounds **2-Co** and **2-Ni**.

Compound	**2-Co**	**2-Ni**
Formula	$C_{18}H_{18}N_4CoO_4S_2$	$C_{18}H_{18}N_4NiO_4S_2$
MW / g mol^{-1}	477.03	477.19
Crystal system	Monoclinic	Monoclinic
Space group	$P2_1/c$	$P2_1/c$
a / Å	14.9459(9)	15.0197(8)
b / Å	9.6273(5)	9.6159(4)
c / Å	15.9668(9)	15.7634(8)
α / °	90	90
β / °	112.032(4)	109.764(4)
γ / °	90	90
V / Å^3	2129.7(2)	2142.56(19)
T / K	293(2)	293(2)
Z	4	4
D_{calc} / g cm^{-3}	1.432	1.479
μ / mm^{-1}	1.058	1.1760
λ / Å	0.7093	0.7093
θ_{max} / deg	2 to 60	2 to 60
R_{wp} / % [a]	4.81	5.21
R_p / % [a]	3.60	3.80
R_{exp} / % [a]	1.55	1.27
R_{Bragg} / % [a]	2.26	2.53

[a] as defined in TOPAS 5.0

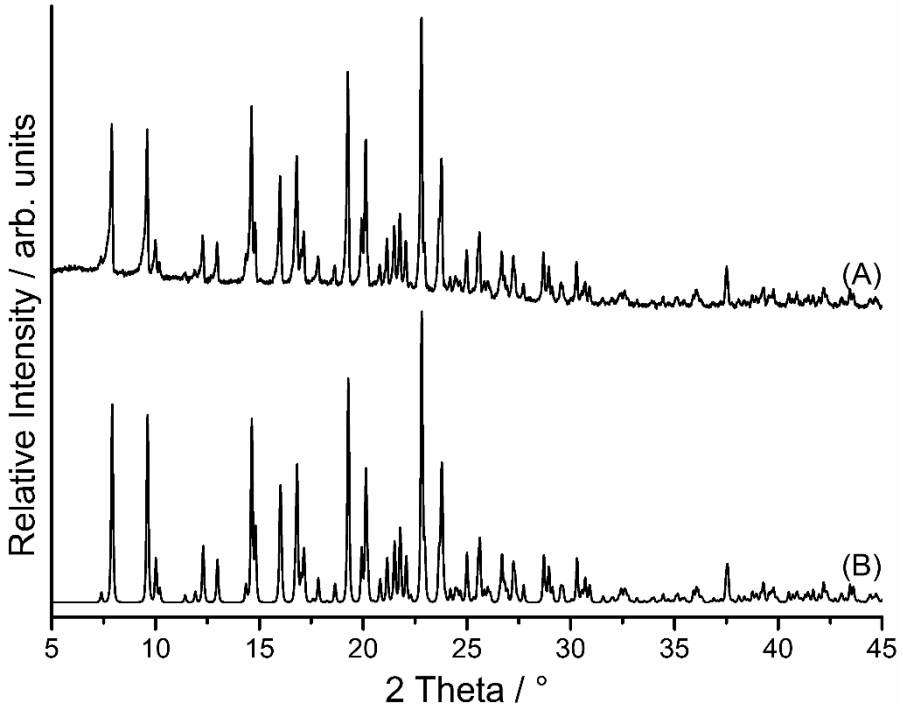

Fig. S1. Experimental (A) and calculated (B) XRPD pattern of **1-Co** (λ = 1.540596 Å).

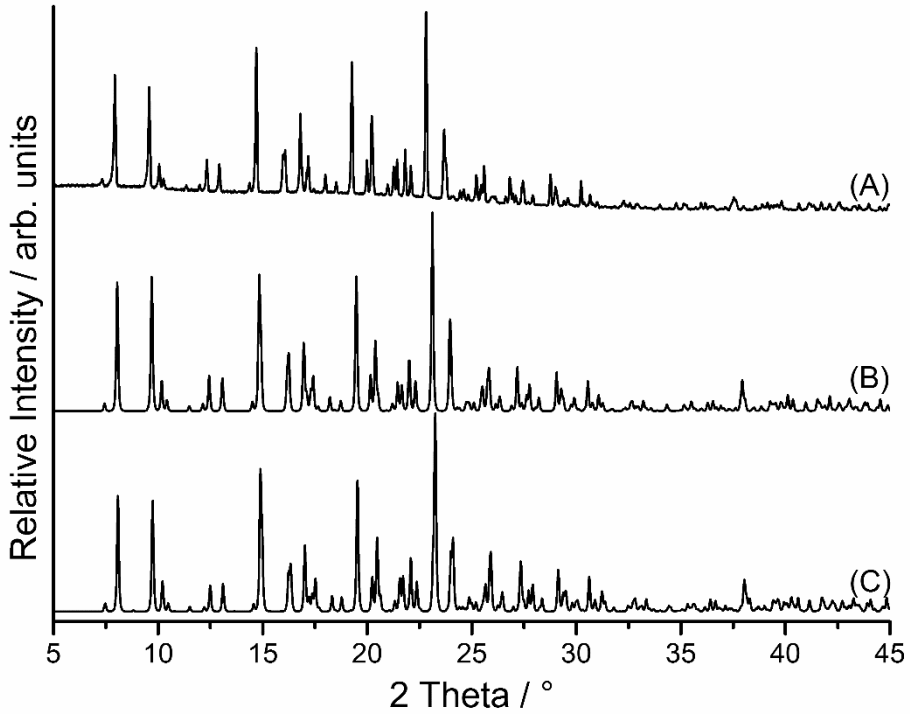

Fig. S2. Experimental (A) and calculated XRPD patterns of **1-Ni** obtained from a new single crystal structure determination at room-temperature (B) and from literature (C) (λ = 1.540596 Å).

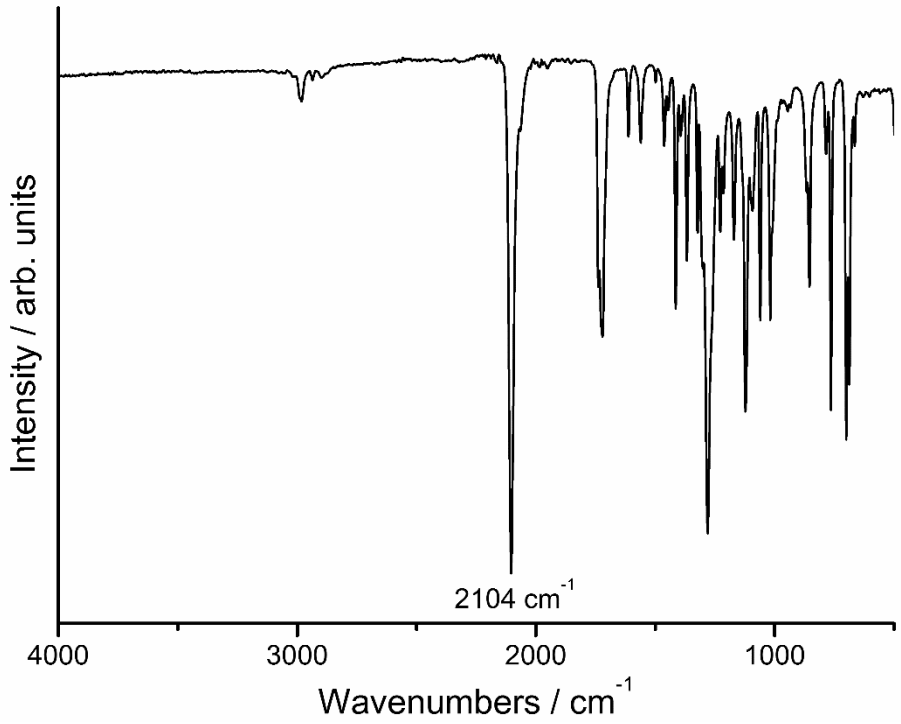

Fig. S3. IR spectrum of **2-Co**. Given is the value for the CN stretching vibration of the thiocyanato anion.

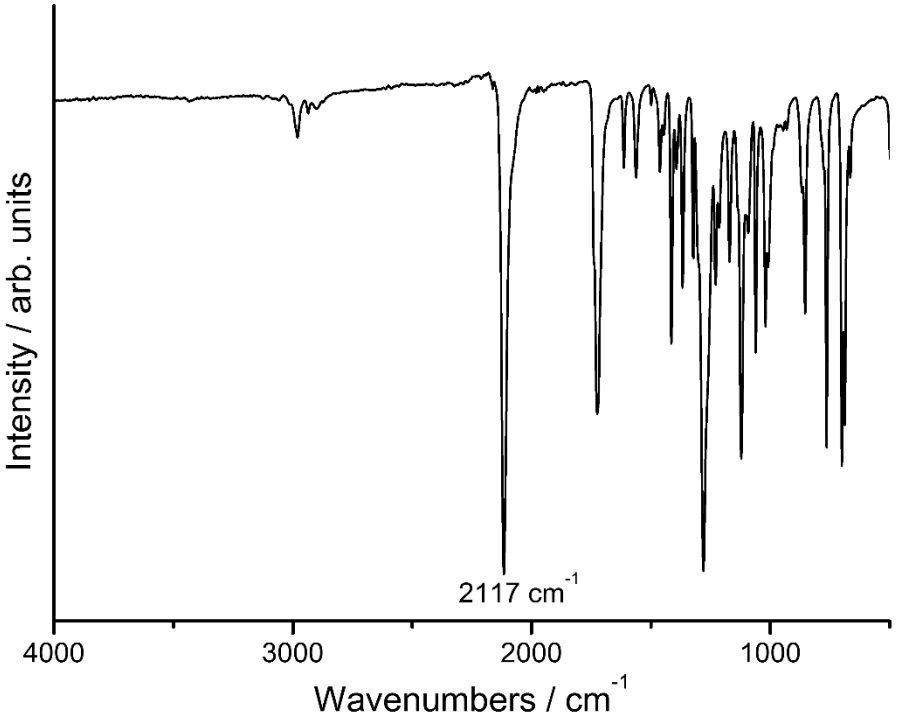

Fig. S4. IR spectrum of **2-Ni**. Given is the value for the CN stretching vibration of the thiocyanato anion.

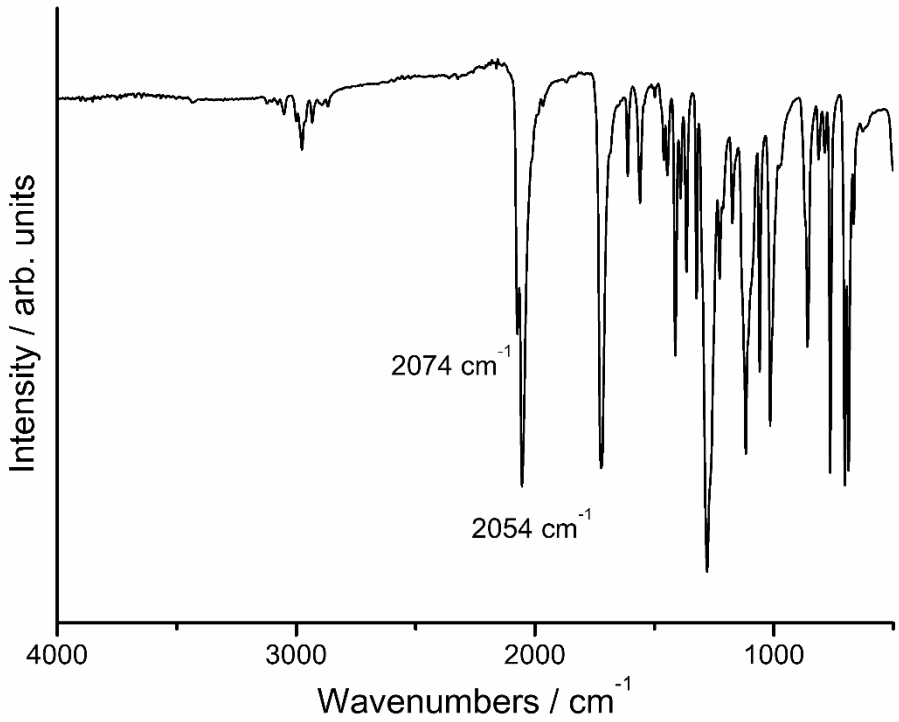

Fig. S5. IR spectrum of **1-Co**. Given are the values for the CN stretching vibrations of the thiocyanato anion.

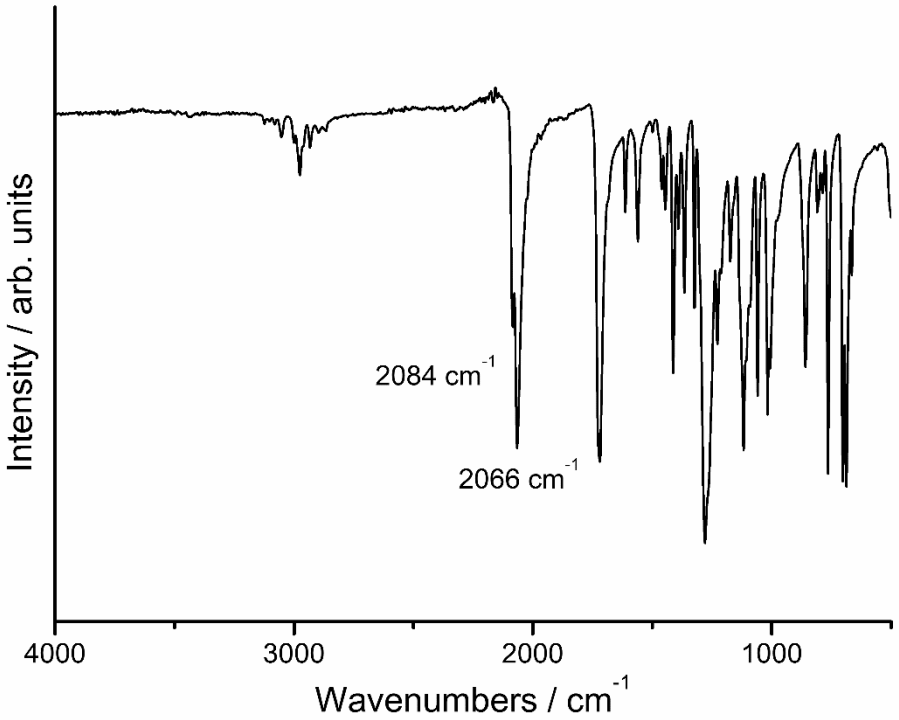

Fig. S6. IR spectrum of **1-Ni**. Given are the values for the CN stretching vibrations of the thiocyanato anion.

Table S3: Selected bond lengths and angles for **2-Ni**.

$Ni(NCS)_2(4\text{-ethylisonicotinate})_2$			
Ni(1)–N(2A)	2.043(2)	Ni(1)–N(11)	2.124(3)
Ni(1)–N(1B)	2.045(2)	Ni(1)–S(2)	2.4896(10)
Ni(1)–N(21)	2.102(3)	Ni(1)–S(1)	2.5568(10)
N(2A)–Ni(1)–N(1B)	175.97(10)	N(21)–Ni(1)–S(2)	90.29(8)
N(2A)–Ni(1)–N(21)	90.26(11)	N(11)–Ni(1)–S(2)	89.60(8)
N(1A)–Ni(1)–N(21)	91.29(10)	N(2A)–Ni(1)–S(1)	85.93(8)
N(2A)–Ni(1)–N(11)	89.93(11)	N(1B)–Ni(1)–S(1)	90.35(8)
N(1A)–Ni(1)–N(11)	88.54(11)	N(21)–Ni(1)–S(1)	90.01(8)
N(21)–Ni(1)–N(11)	179.79(11)	N(11)–Ni(1)–S(1)	90.11(8)
N(2A)–Ni(1)–S(2)	91.06(8)	S(2)–Ni(1)–S(1)	176.98(3)
N(1B)–Ni(1)–S(2)	92.66(8)		

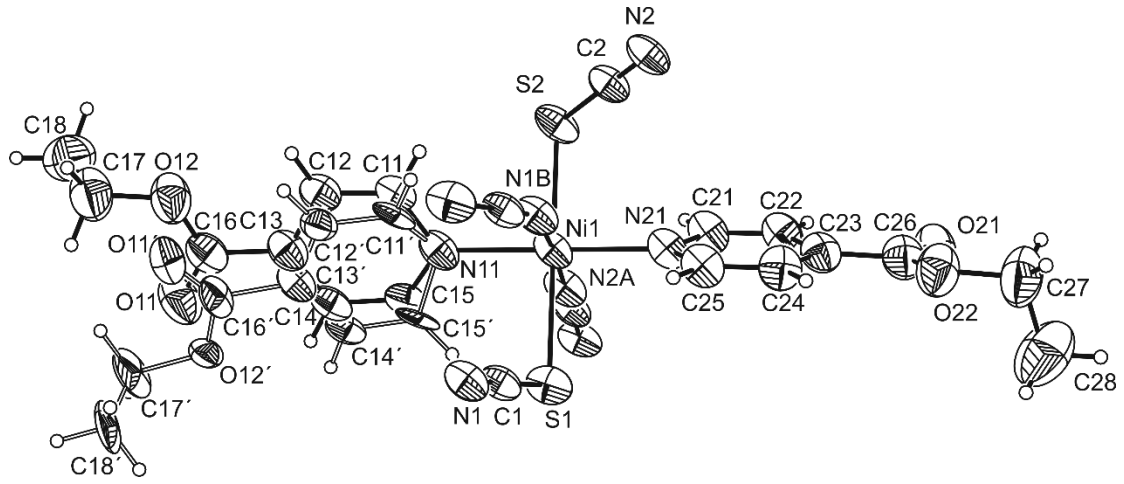

Fig. S7. ORTEP plot of **2-Ni** with labeling displacement ellipsoids drawn at the 50% probability level.

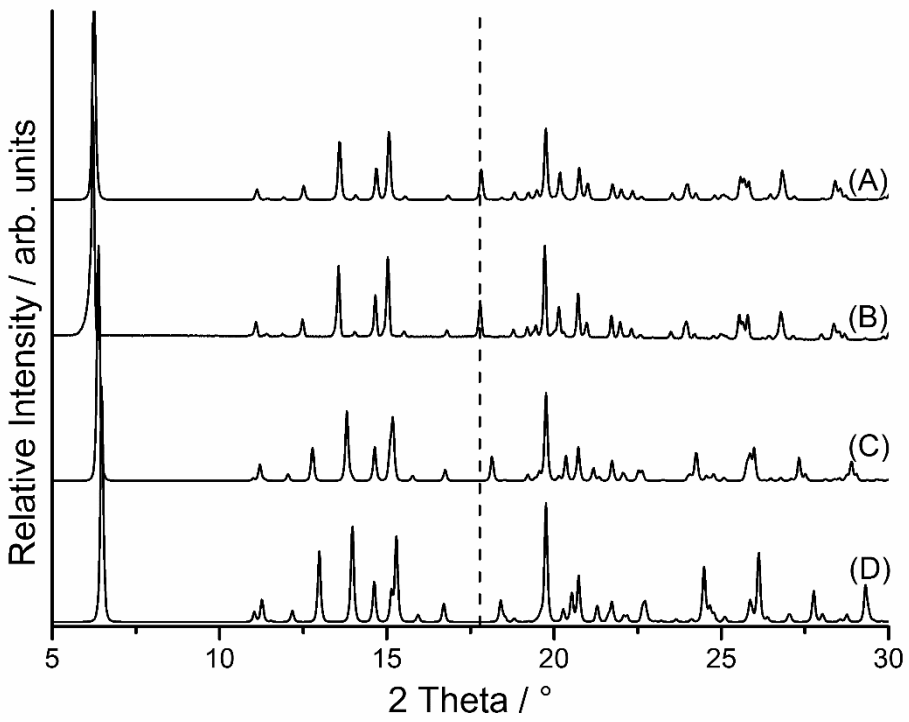

Fig. S8. XRPD patterns of **2-Ni** calculated from the Rietveld refinement (A), experimental XRPD pattern of **2-Ni** (B) and XRPD pattern of **2-Ni** calculated from single crystal data at room temperature (C) and at 170 K (D) (λ = 1.540596 Å).

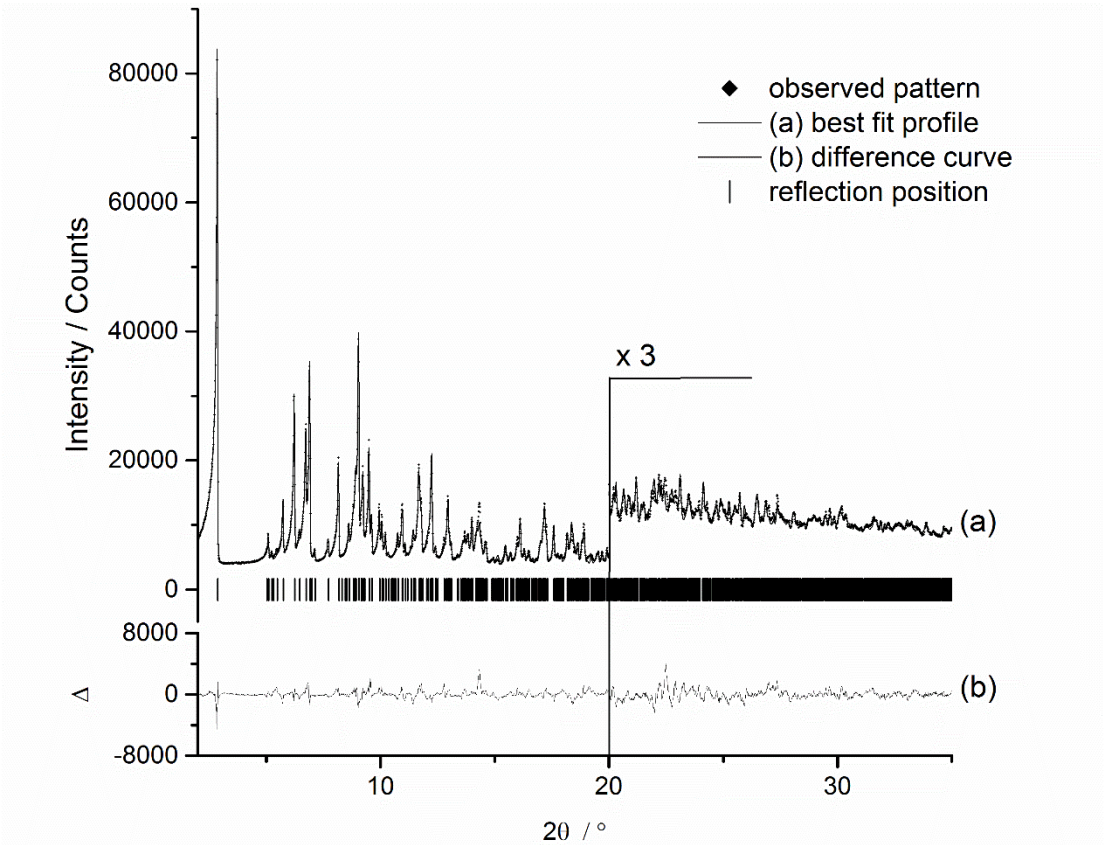

Fig. S9. Difference plot of **2-Ni** with calculated pattern shown as diamonds, best fit as black curve with the difference curve bellow (λ = 0.7093 Å).

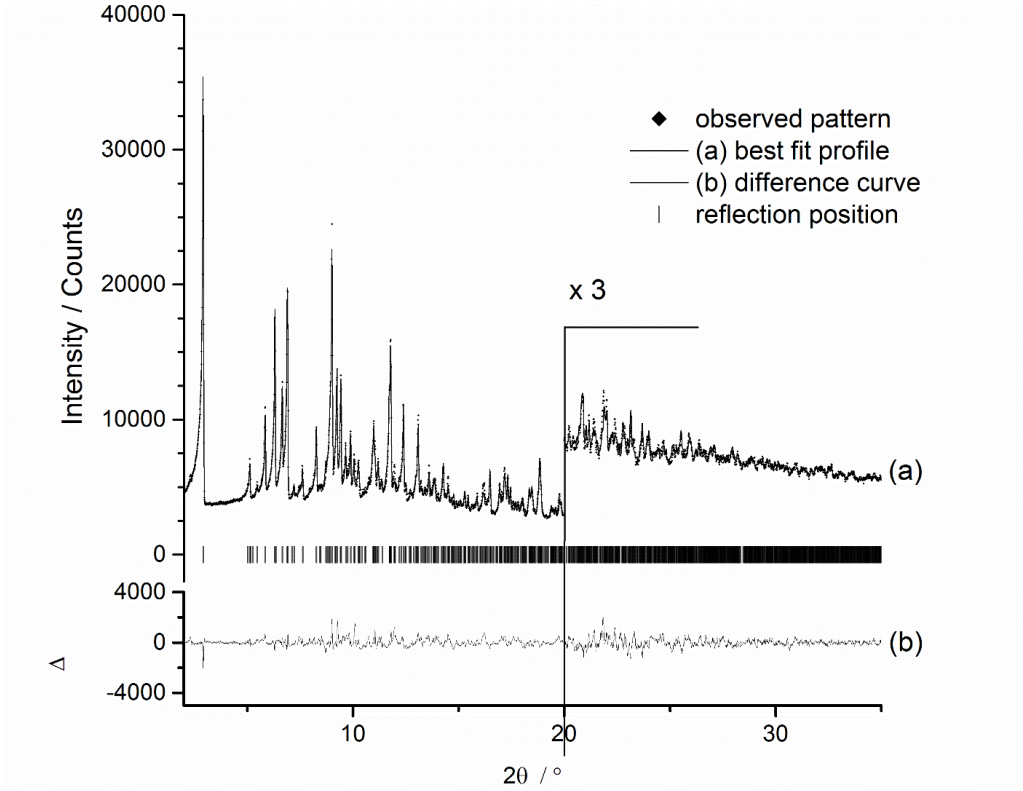

Fig. S10. Difference plot of **2-Co** with calculated pattern shown as diamonds, best fit as black curve with the difference curve bellow (λ = 0.7093 Å).

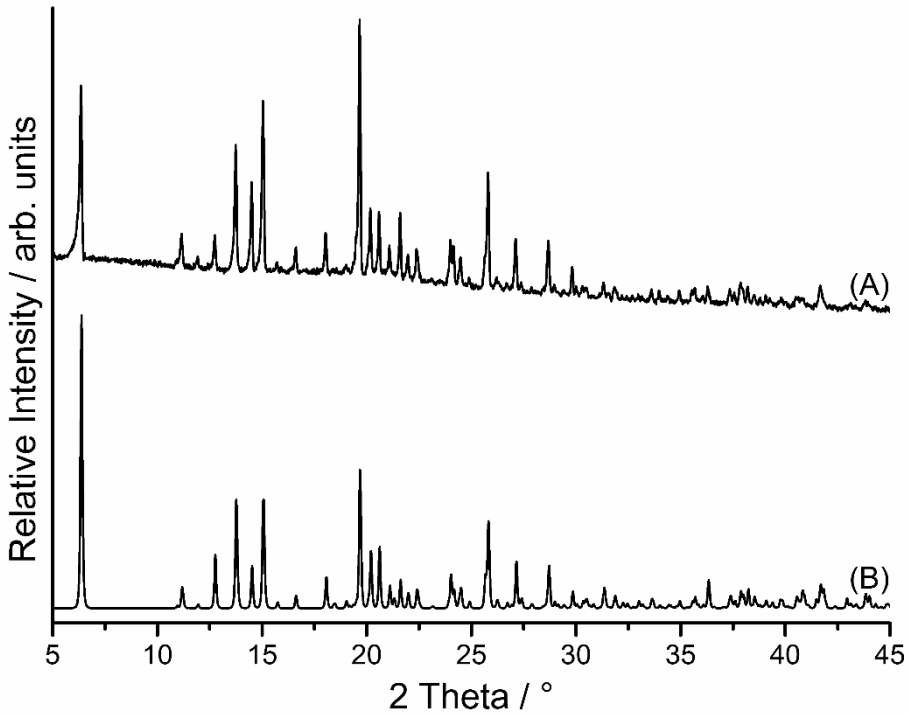

Fig. S11. Experimental (A) and calculated (B) XRPD patterns of **2-Co** (λ = 1.540596 Å).

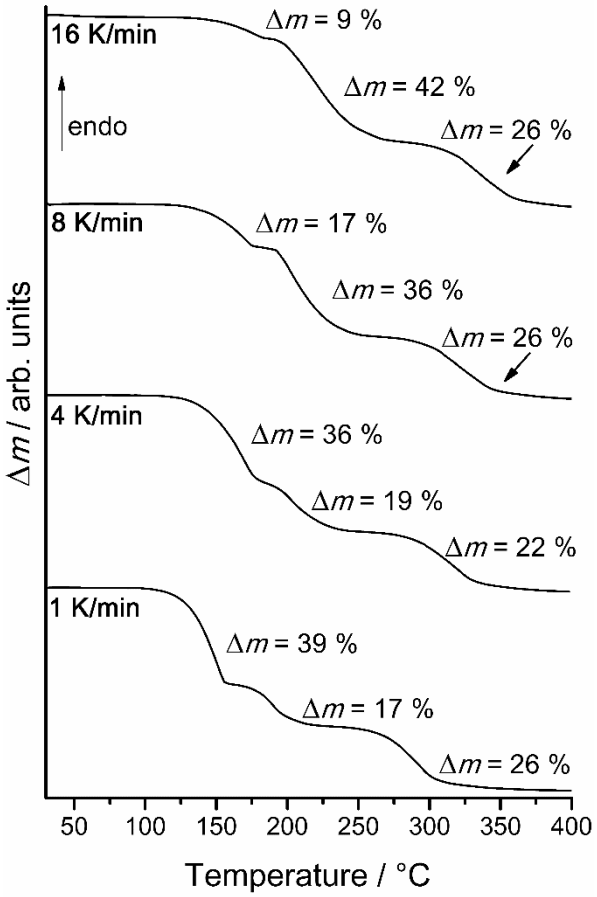

Fig. 3. Heating rate dependent TG measurements for **1-Co**.

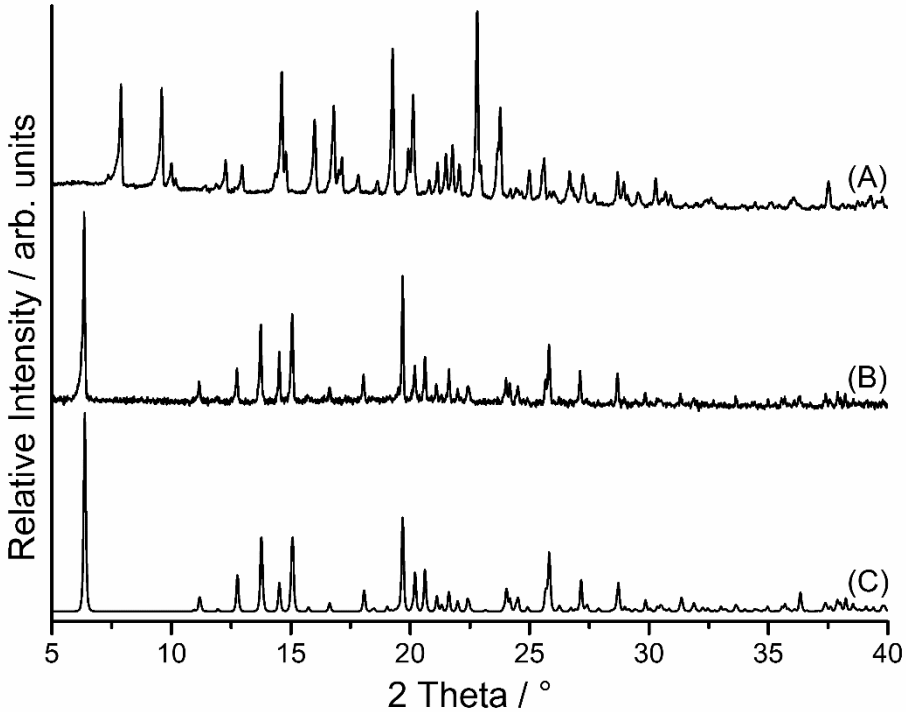

Fig. S13. Experimental XRPD patterns of **1-Co** (A), the residue obtained after the first mass step of **1-Co** (B), and the calculated XRPD pattern of **2-Co** (C) (λ = 1.540596 Å).

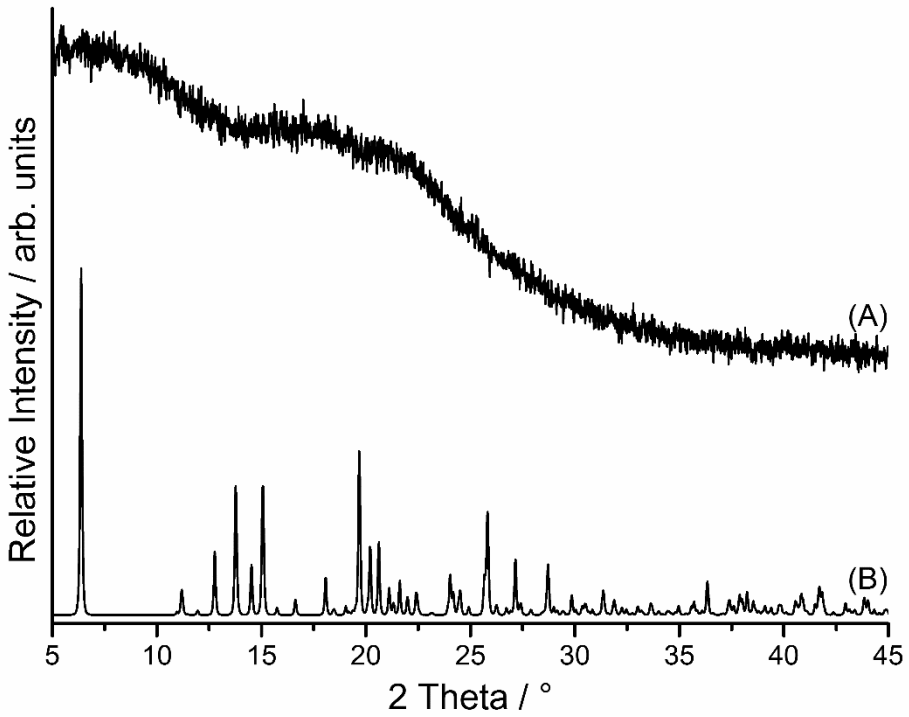

Fig. S14. Experimental XRPD patterns of the residue obtained after the second mass step of **1-Co** (A), and the calculated XRPD pattern of **2-Co** (B) (λ = 1.540596 Å).

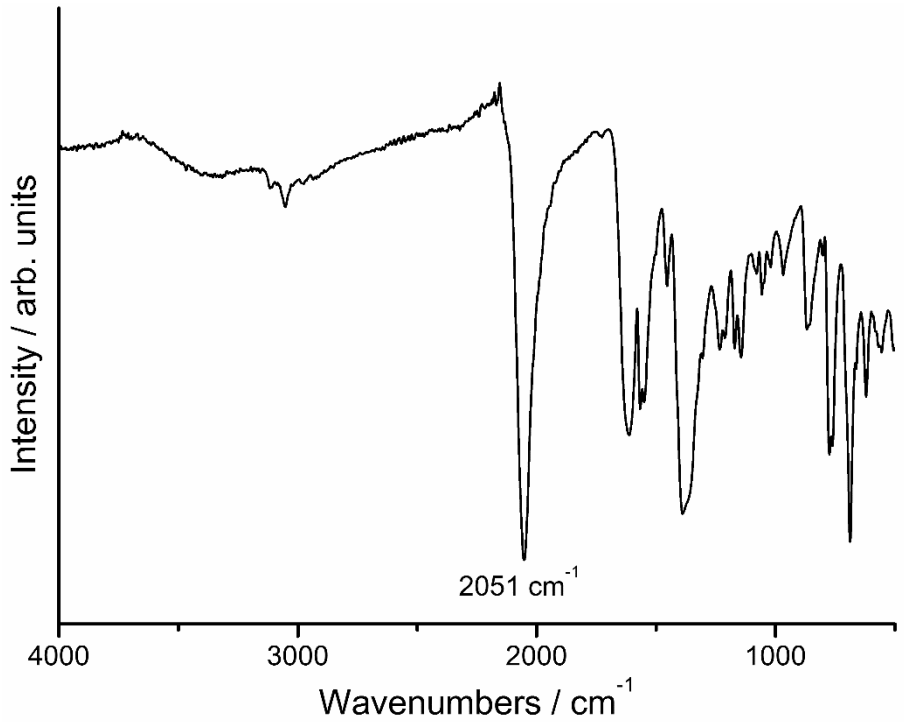

Fig. S15 IR spectra of the residue obtained after the second mass step of **1-Co**. Given is the value for the CN stretching vibration of the thiocyanato anion.

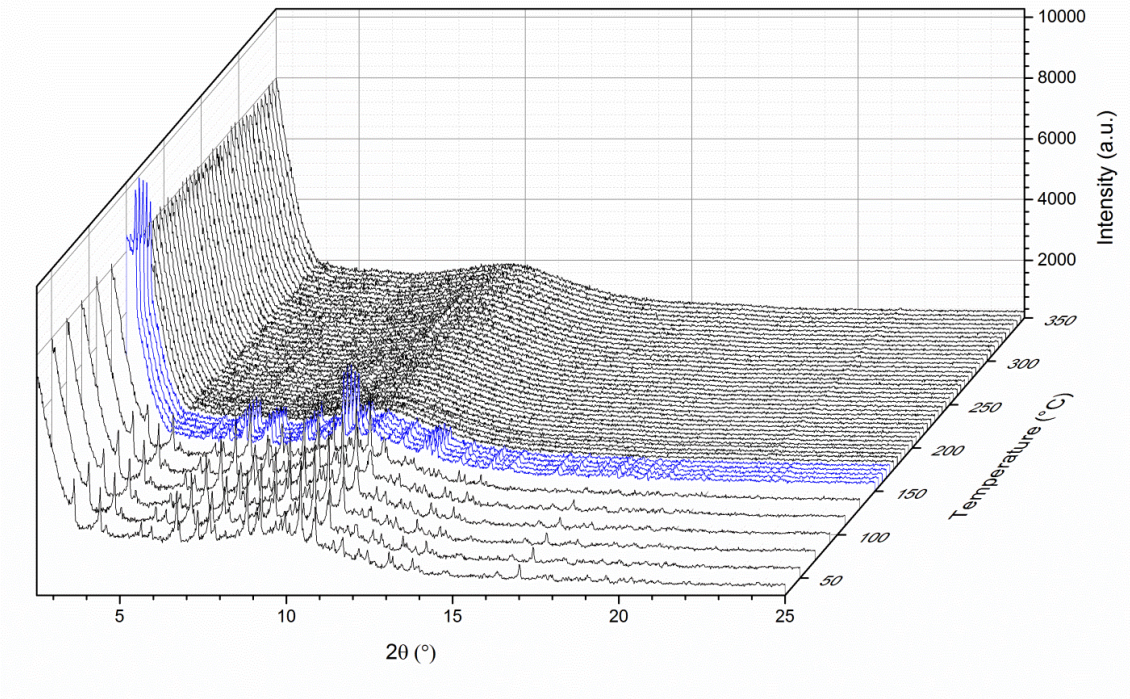

Fig. S16. Temperature dependent XRPD measurement for **1-Co**. The different phases are colored in black (**1-Co**) and blue (**2-Co**), respectively. Above 180 °C no intensity was observed (λ = 0.7093 Å).

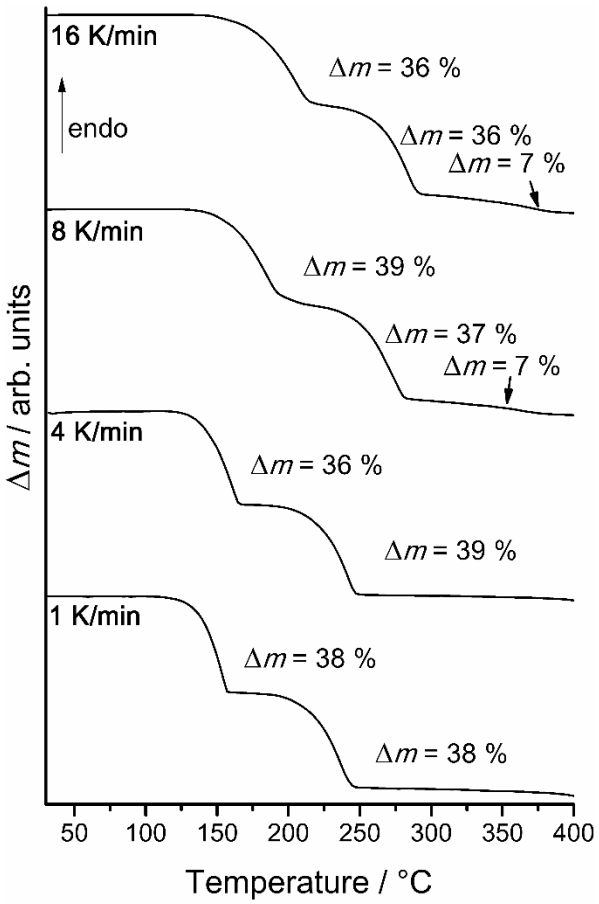

Fig. S17. Heating rate dependent TG curves for **1-Ni**.

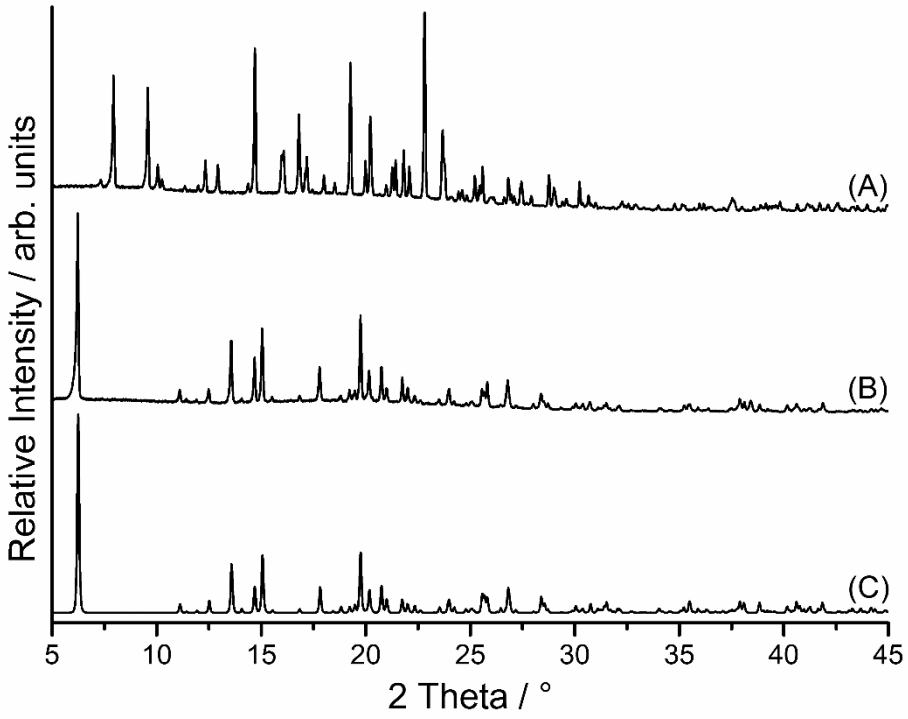

Fig. S18. Experimental XRPD patterns of **1-Ni** (A), the residue obtained after the first mass step of **1-Ni** (B) and the calculated XRPD pattern of **2-Ni** (C) (λ = 1.540596 Å).

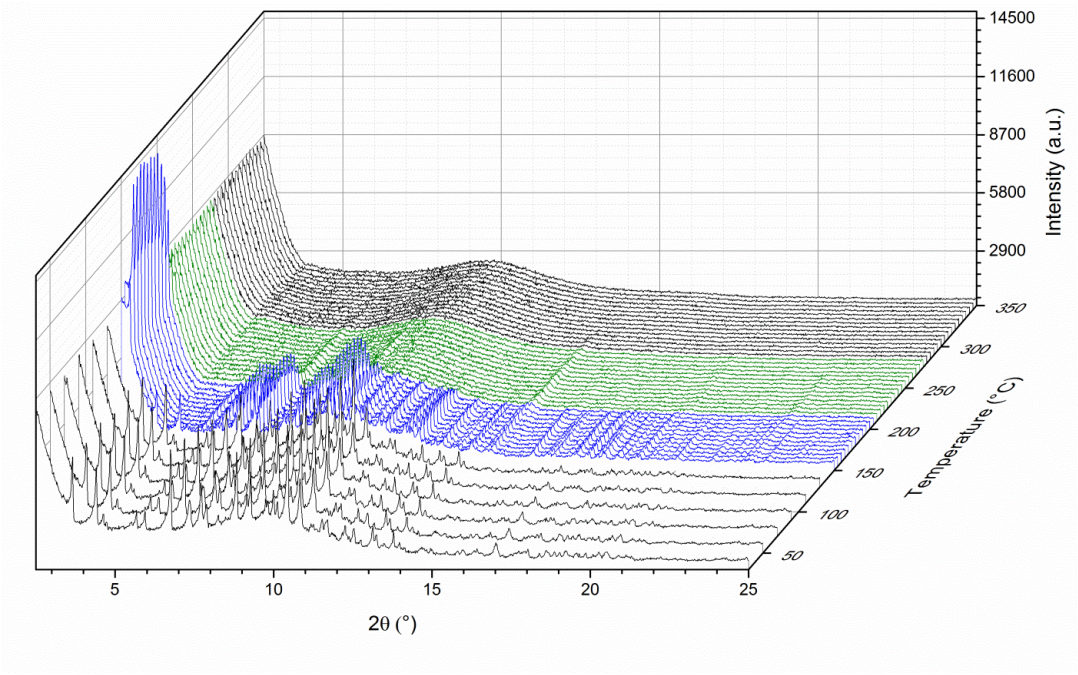

Fig. S19. Temperature dependent XRPD measurement for **1-Ni**. The different phases are colored in black (**1-Ni**), blue (**2-Ni**) and green (nickel thiocyanate complex), respectively. Above 290 °C no intensity was observed (λ = 0.7093 Å).

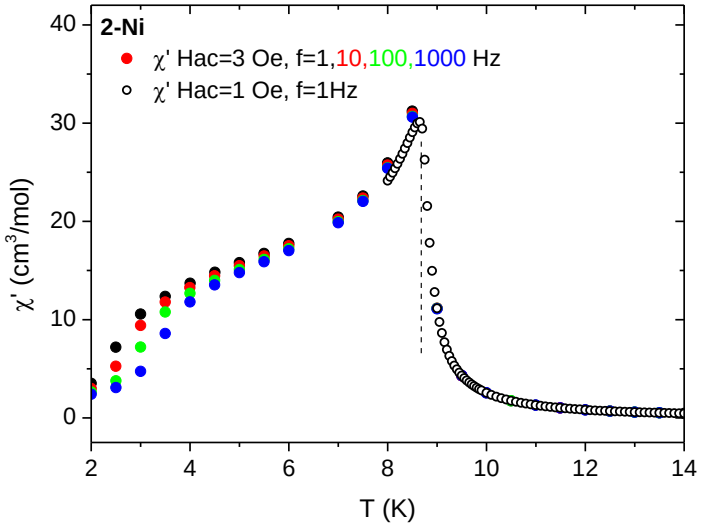

Fig. S20. The in-phase component χ' of AC susceptibility measured for **2-Ni** using different AC frequencies. The dashed line is drawn at T_c = 8.70 K as determined from specific heat measurements.

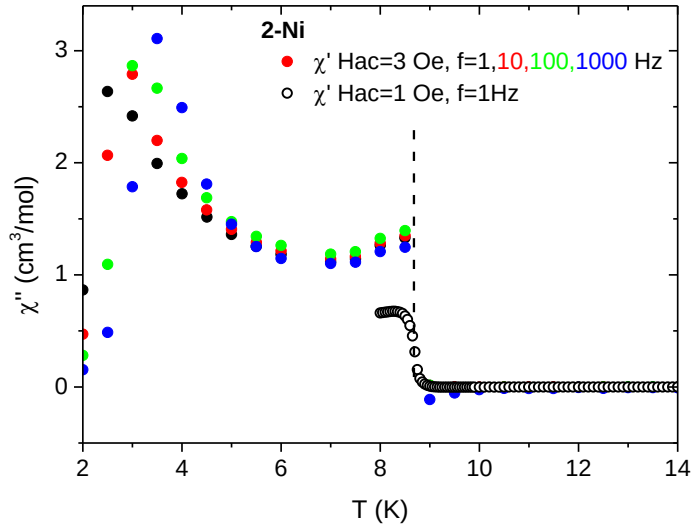

Fig. S21. The out-of-phase component χ'' of AC susceptibility measured for **2-Ni** using different AC frequencies. The dashed line is drawn at 8.70 K in all related figures.

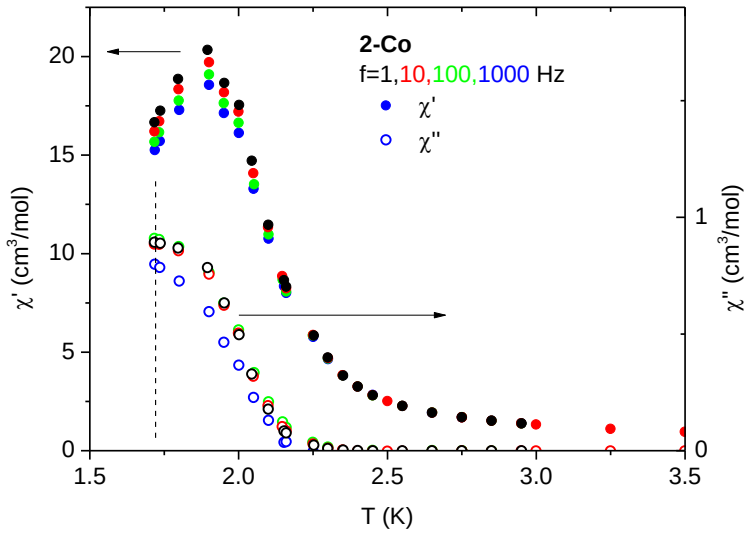

Fig. S22. AC susceptibility measured for **2-Co**. The dashed line is drawn at T_c = 1.72 K as determined from specific heat measurements. The maximum of χ' is slightly above T_c.

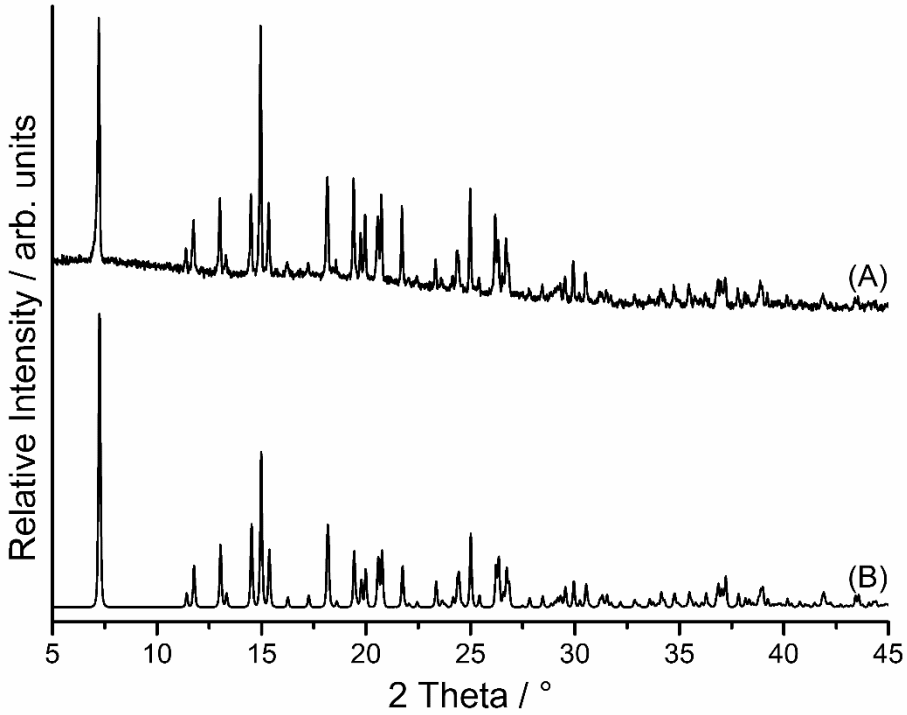

Fig. S23. Experimental (A) and calculated (B) XRPD patterns for 2D $[Co(NCS)_2(4\text{-acetylpyridine})_2]_n$ (λ = 1.540596 Å).

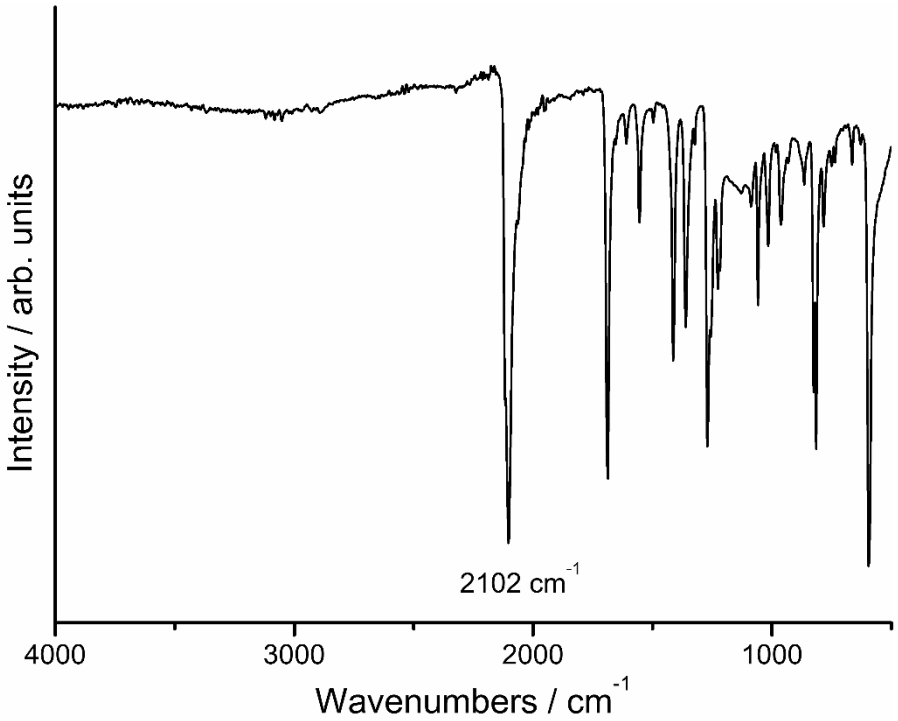

Fig. S24. IR spectra for 2D $[Co(NCS)_2(4\text{-acetylpyridine})_2]_n$. Given is the value for the CN stretching vibration of the thiocyanato anion.

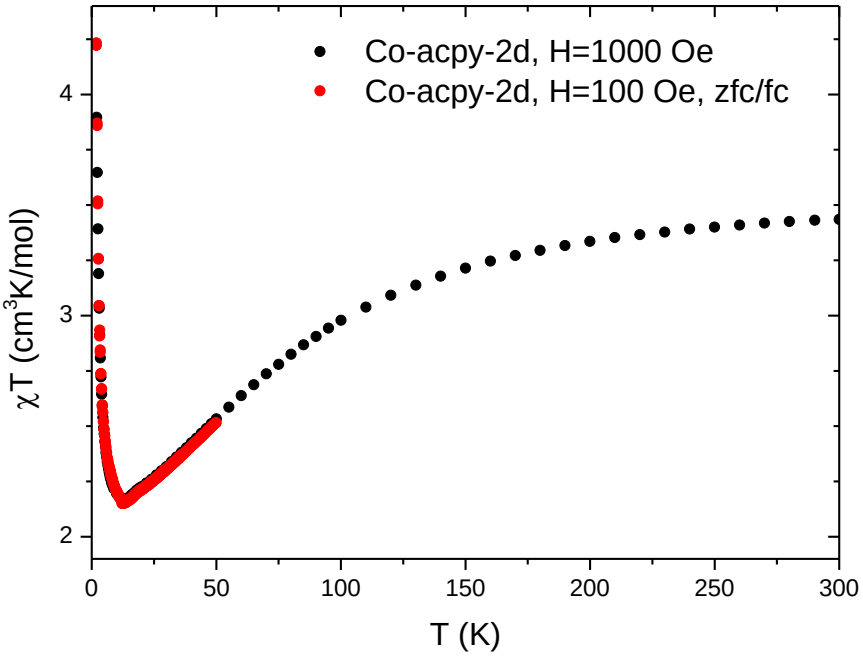

Fig. S25. Magnetic susceptibility as function of temperature of $Co(NCS)_2(4\text{-acetylpyridine})_2]_n$ measured at 100 and 1000 Oe.

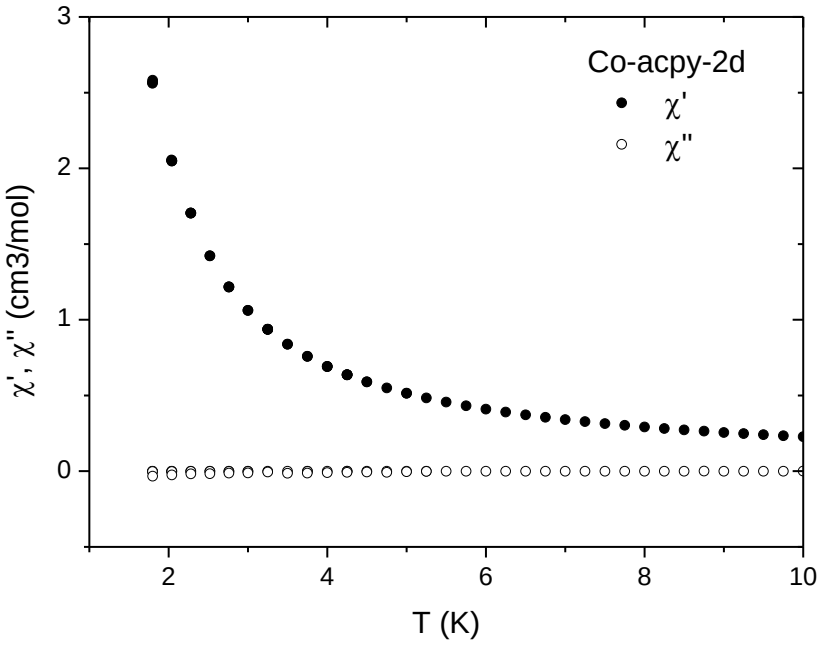

Fig. S26. AC susceptibility as function of temperature of $Co(NCS)_2(4\text{-acetylpyridine})_2]_n$ measured at frequencies from 10 to 1000 Hz.

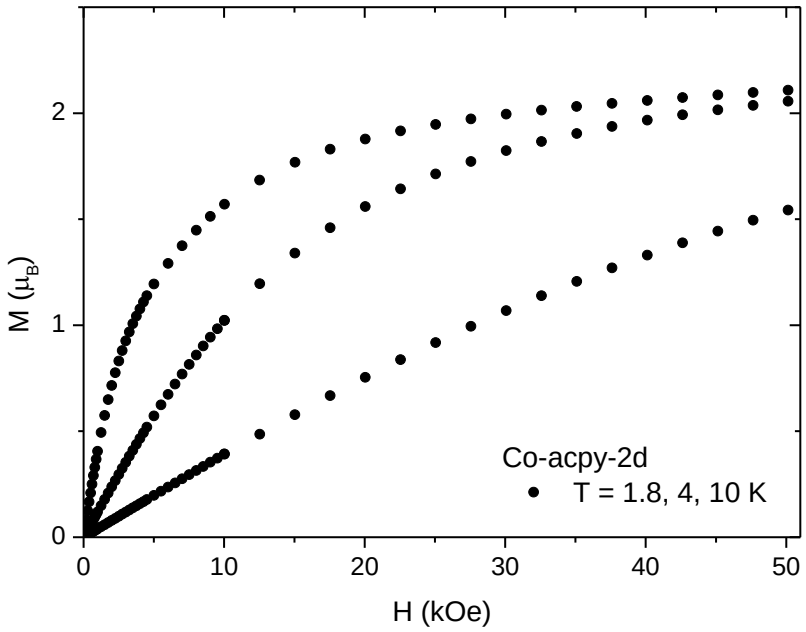

Fig. S27. Magnetization measurements of $Co(NCS)_2(4\text{-acetylpyridine})_2]_n$ at different temperatures.

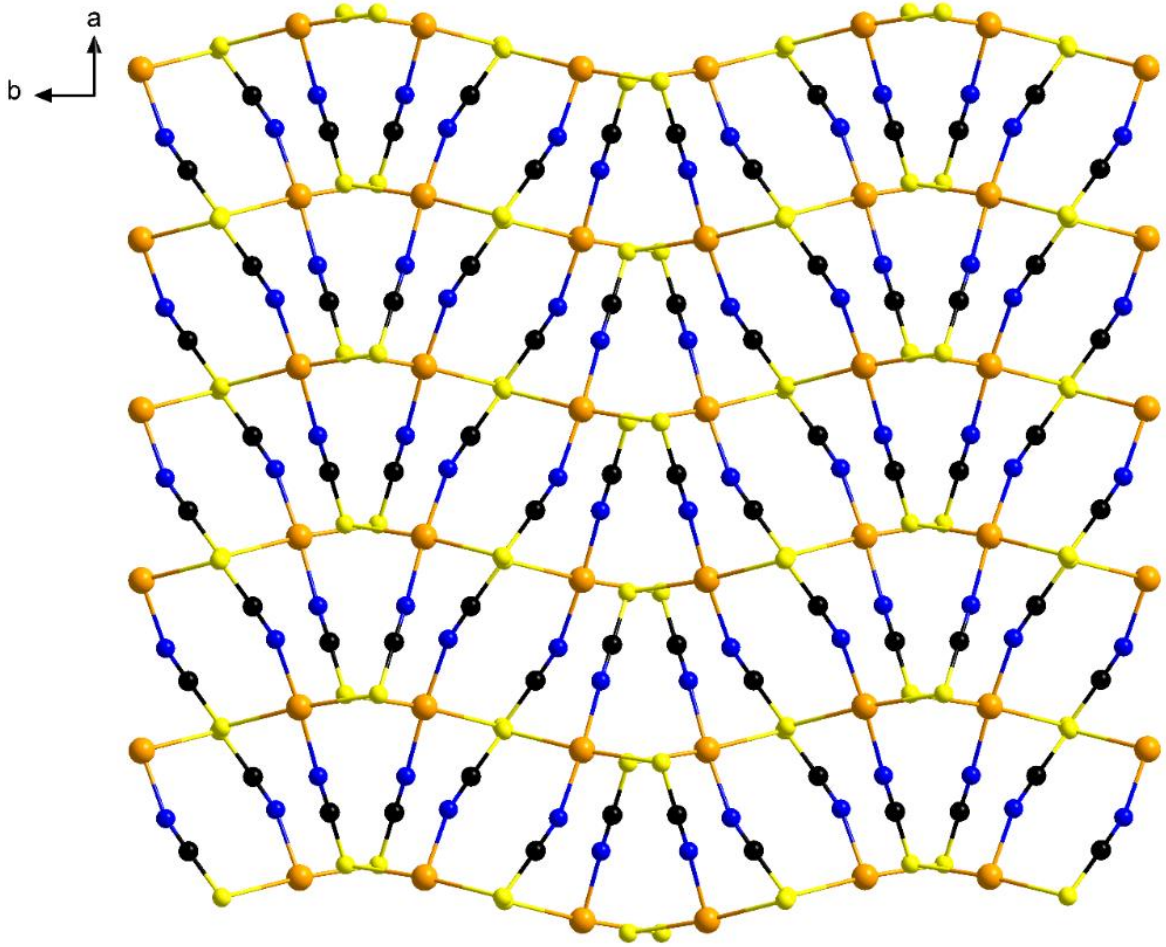

Fig. S28. View of the stacking of two layers in 2D $[Co(NCS)_2(4\text{-acetylpyridine})_2]_n$ along the crystallographic *c* axis.

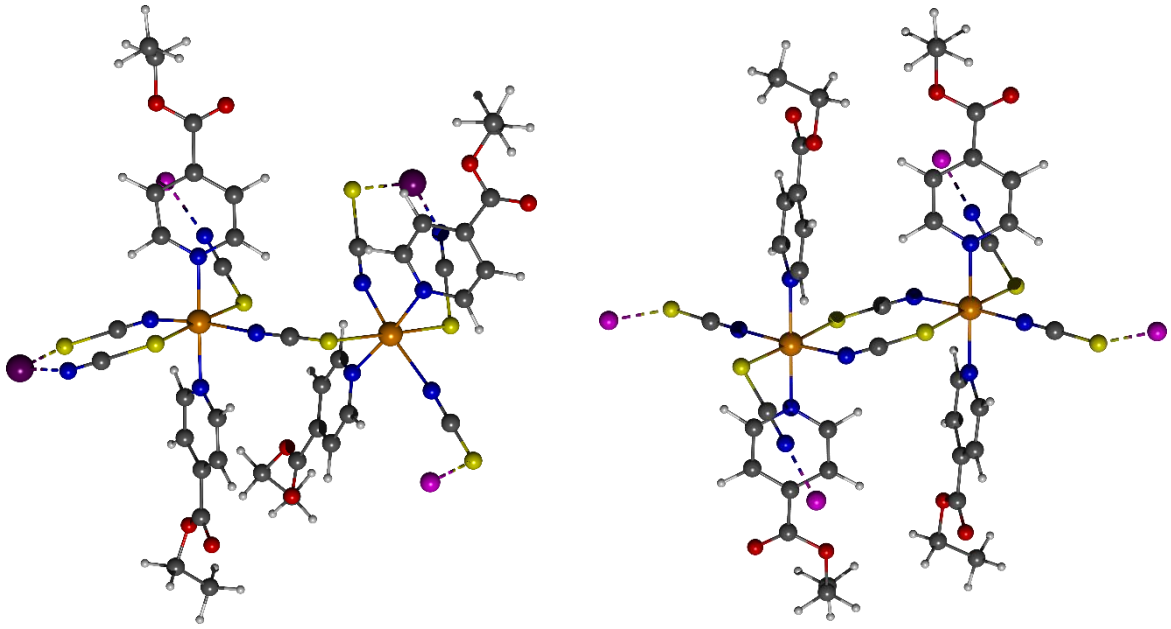

Fig. S29. Dinuclear model systems 1 (left) and 2 (right) for the two bridging modes observed in **2-Ni** and **2-Co** utilized in the CDFT calculations to obtain J_1 and J_2, respectively. Pink (purple) spheres designate point charges of +0.5 (+1.0) to compensate negative charge of the fragments.

Table S4. CDFT Results for **2-Ni** and **2-Co**. Magnetic coupling constants have been calculated by equation (1).

			J / K	State	$2S$+1	E_{rel} / a.u.	$\langle S^2 \rangle$
2-Ni	(single crystal)	J_1	10.5	HS	5	−8515.871446	6.0206
				BS	1	−8515.871181	2.0199
		J_2	7.7	HS	5	−8024.662003	6.0158
				BS	1	−8024.661809	2.0156
2-Ni	(Rietveld)	J_1	3.2	HS	5	−8516.134861	6.0189
				BS	1	−8516.134780	2.0189
		J_2	−14.2	HS	5	−8024.503091	6.0182
				BS	1	−8024.503450	2.0116
2-Co	(Rietveld)	J_1	40.9	HS	7	−8264.744437	12.0311
				BS	1	−8264.742108	3.0292
		J_2	19.3	HS	7	−7773.057242	12.0302
				BS	1	−7773.056142	3.0266
2-Co	(**2-Ni** single crystal)	J_1	−42.2	HS	7	−8264.744373	12.0311
				BS	1	−8264.746777	3.0280
		J_2	−9.4	HS	7	−7773.541874	12.0263
				BS	1	−7773.542412	3.0247

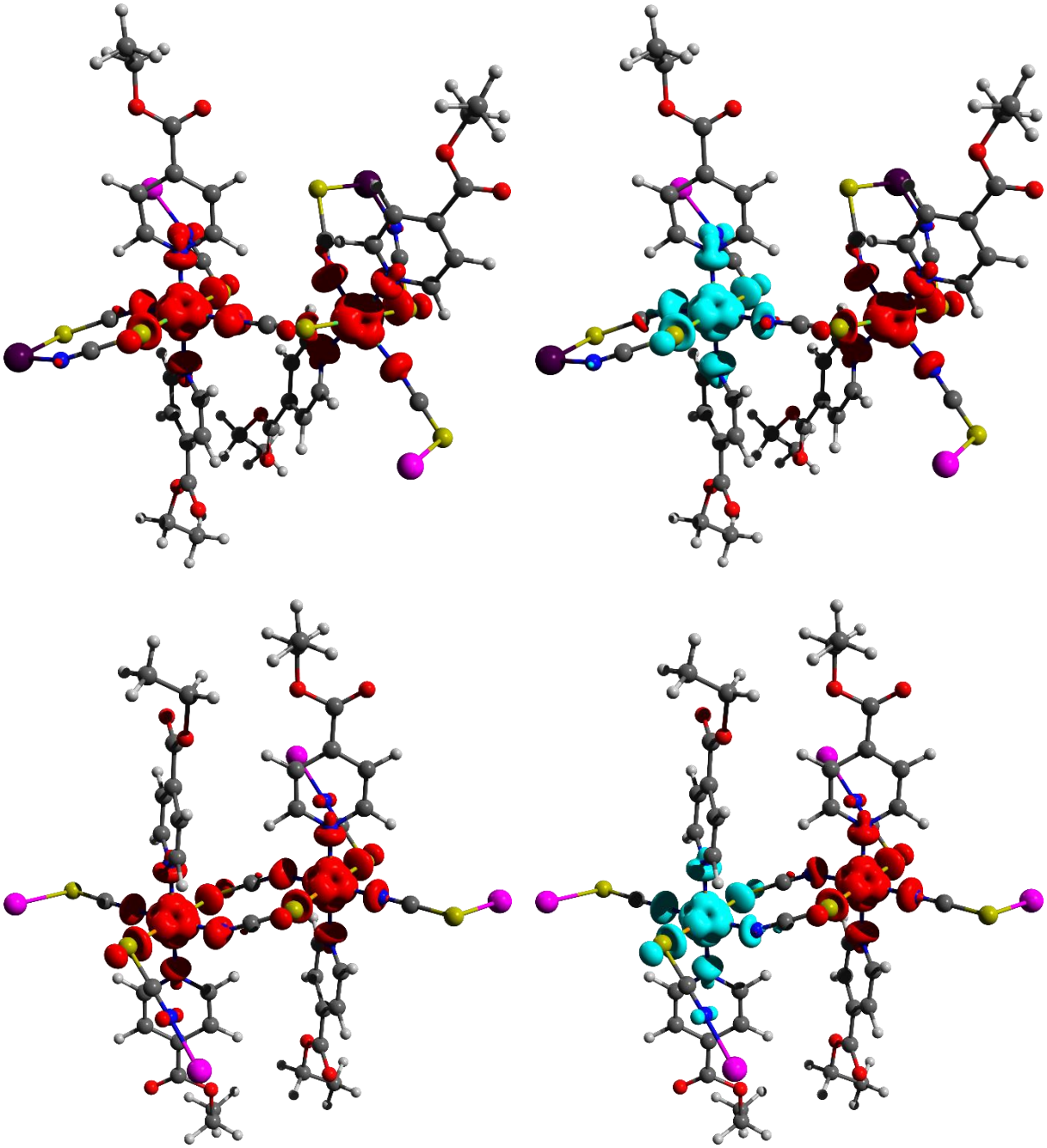

Fig. S30. CDFT spin densities of **2-Ni** for high-spin (left column) and broken-symmetry (right column) states. Red (cyan) isosurfaces represent net α (β) spin densities (iso-value 0.004). First and second row represents the computational model for magnetic coupling constants J_1 and J_2, respectively.

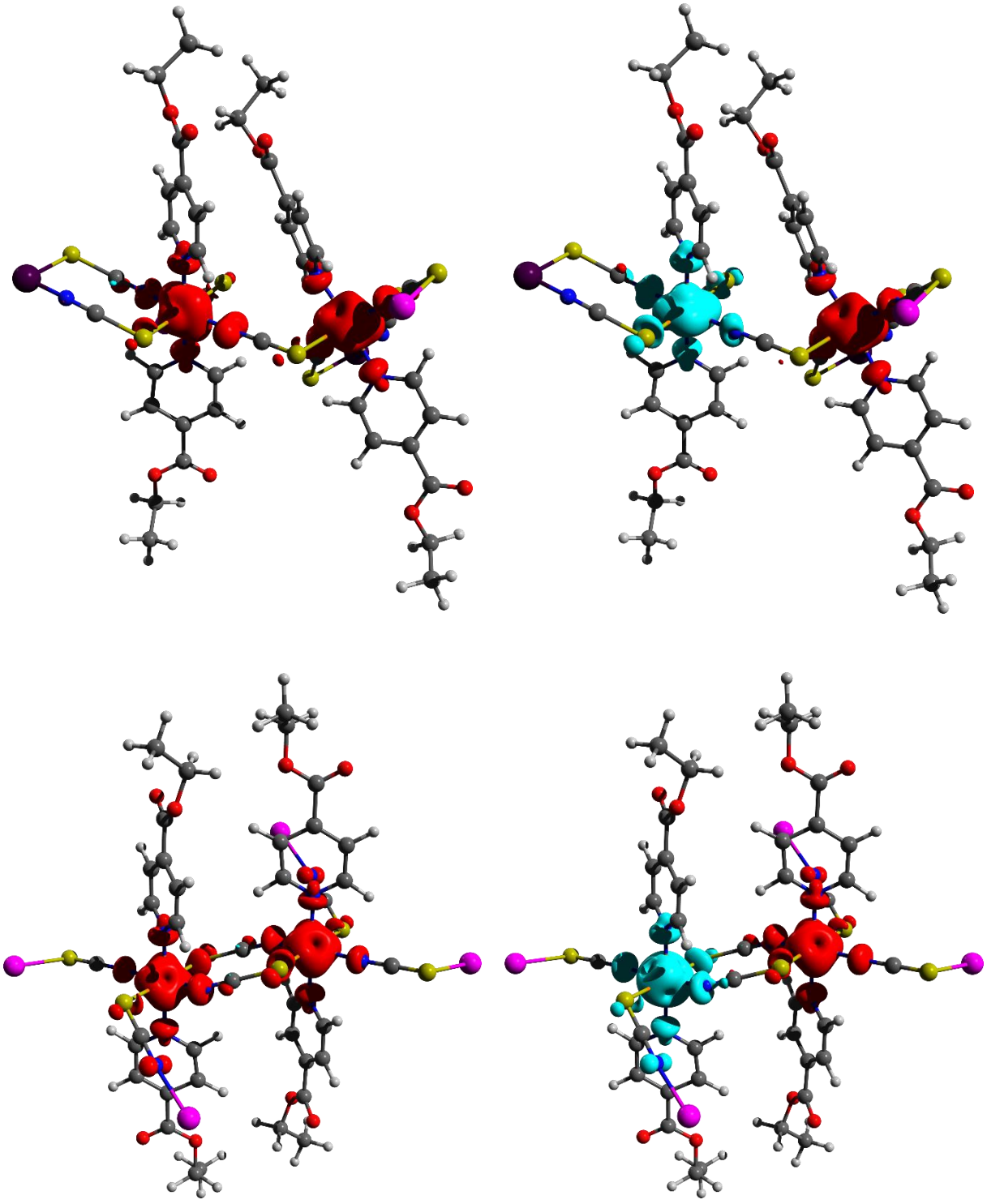

Fig. S31. CDFT spin densities of **2-Co** for high-spin (left column) and broken-symmetry (right column) states. Red (cyan) isosurfaces represent net α (β) spin densities (iso-value 0.004). First and second row represents the computational model for magnetic coupling constants J_1 and J_2, respectively.

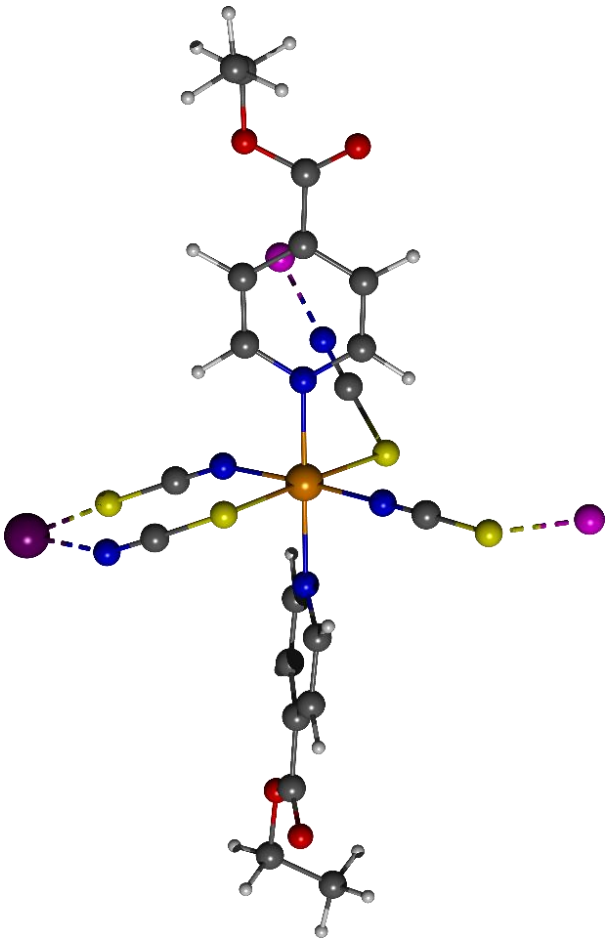

Fig. S32. Computational model used for the *ab initio* calculations. Pink and purple spheres designate point charges of +0.5 and +1.0, respectively, to compensate negative charges of the fragment.

Table S5. Relative CASSCF and CASPT2 energies (in cm^{-1}) for **2-Ni** and **2-Co**.

		2-Ni (single crystal)				**2-Co** (Rietveld)	
2*S*+1	Term	CASSCF	CASPT2	2*S*+1	Term	CASSCF	CASPT2
3	^{3}F	0	0	4	^{4}F	0	0
		6884	8076			198	172
		7029	8171			436	469
		9494	10823			5887	7088
		12792	13522			9457	10681
		13952	15801			9863	11012
		14186	16090			18372	20885
	^{3}P	27084	24800		^{4}P	22733	20627
		28703	25802			22951	20942
		28956	25912			27397	25292
1	^{1}D	17247	14131	2	^{2}G + ^{2}P	9144	5956
		18107	14768			14335	11050
		24411	22725			16455	14323
		24479	22740			16849	14547
		26549	24830			18818	15940
	^{1}G	29236	24570			19611	16583
		29342	27218			20002	16924
		32673	30221			21226	18028
		33043	30615			23814	20471
		36606	35889			24127	20869
		37198	36398			24769	20583
		37336	36738			25431	23790
		37438	36875		…	…	…
		38092	37190				
	^{1}S	68420	55750				

Table S6. Relative RASSI-SO energies (in cm^{-1}) for the lowest spin-orbit coupled states in **2-Ni** and **2-Co** whereas in the latter case degenerated Kramers doublets (KDs) are obtained.

		2-Ni (single crystal)			**2-Co** (Rietveld)
Subterm	State	E_{rel} / cm^{-1}	Subterm	KD State	E_{rel} / cm^{-1}
$^3A_{2g}$	1	0.0	$^4T_{1g}$	1	0.0
	2	9.4		2	260.1
	3	10.1		3	464.5
				4	868.3
				5	1005.4
				6	1146.3

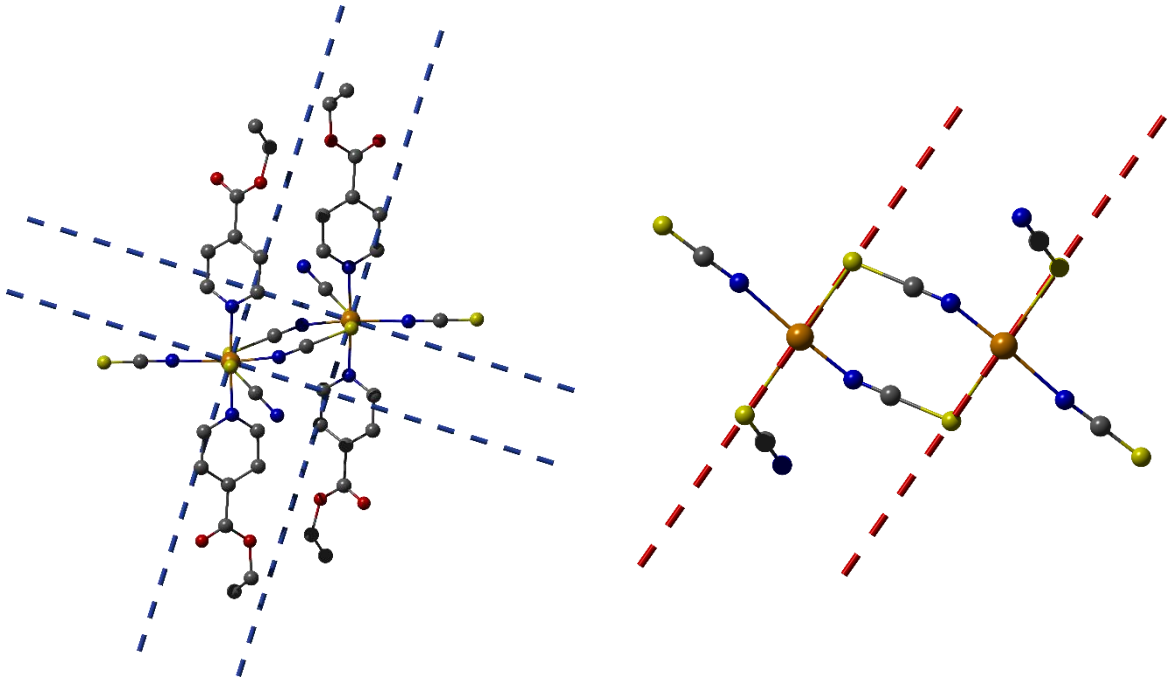

Fig. S33. *Ab initio* calculated (S_{eff} =1/2) magnetic axes (blue dashed lines: axes defining the easy-plane; red dashed lines: hard-axes) for the first excited KD state of **2-Co** projected onto a dinuclear Co(II) fragment. Hydrogen atoms as well as pyridine-based co-ligands in top view (right) are omitted for clarity.

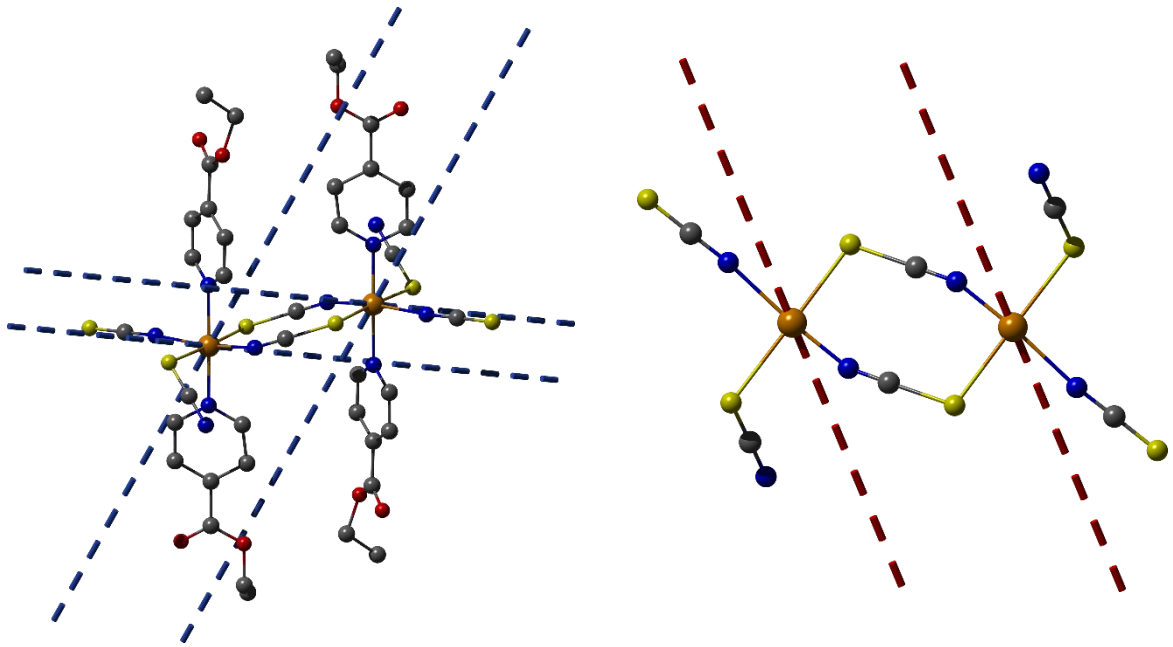

Fig. S34. *Ab initio* calculated (S_{eff} =3/2) anisotropy axes (blue dashed lines: easy-axes; red dashed lines: hard-axes) for the two lowest KD states of **2-Co** projected onto a dinuclear Co(II) fragment. Hydrogen atoms as well as pyridine-based co-ligands in top view (right) are omitted for clarity.

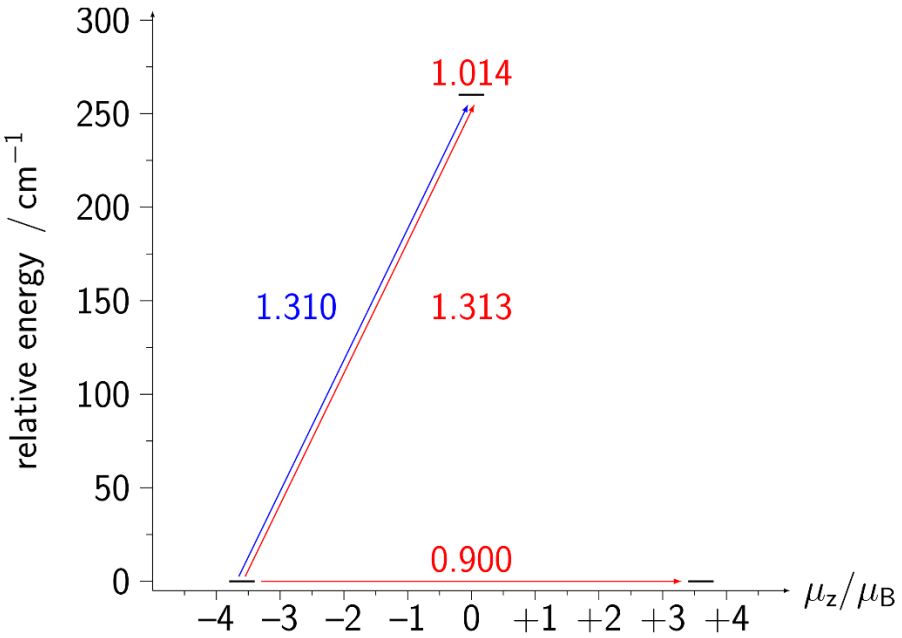

Fig. S35. Magnetization blocking barriers in **2-Co**. Arrows represent the transition between different magnetic states and corresponding values show the average dipole matrix element $\bar{\mu}_z$ in respect to the ground state easy-axis orientation.

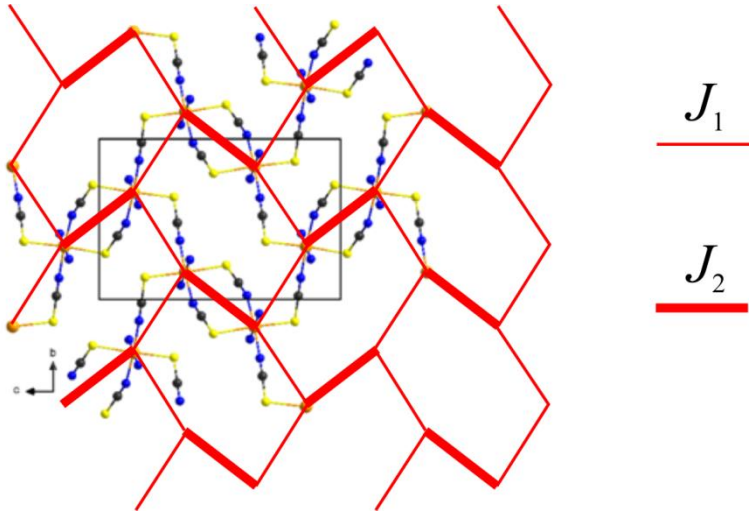

Fig. S36. Deformed chicken-wire lattice of exchange interaction paths between S = 1 spins of Ni(II), as used in quantum Monte Carlo simulations to calculate magnetic susceptibility of **2-Ni**.